The Planetary Science Journal, 6:107 (12pp), 2025 May https://doi.org/10.3847/PSJ/adc390

Improved Carbon and Nitrogen Isotopic Ratios for CH_3CN in Titan's Atmosphere Using ALMA

Jonathon Nosowitz[1,2], Martin A. Cordiner[1,2], Conor A. Nixon[2], Alexander E. Thelen[3], Zbigniew Kisiel[4], Nicholas A. Teanby[5], Patrick G. J. Irwin[6], Steven B. Charnley[2], and Véronique Vuitton[7]
[1] Department of Physics, The Catholic University of America, Washington, DC 20064, USA; nosowitz@cua.edu
[2] Solar System Exploration Division, NASA Goddard Space Flight Center, Greenbelt, MD 20771, USA
[3] Division of Geological and Planetary Sciences, California Institute of Technology, Pasadena, CA 91125, USA
[4] Institute of Physics, Polish Academy of Sciences, Al. Lotników 32/46, 02-668 Warszawa, Poland
[5] School of Earth Sciences, University of Bristol, Bristol BS8 1RJ, UK
[6] Atmospheric, Oceanic and Planetary Physics, Clarendon Laboratory, University of Oxford, Oxford OX1 3PU, UK
[7] Univ. Grenoble Alpes, CNRS, IPAG, 38000 Grenoble, France
Received 2024 October 18; revised 2025 March 3; accepted 2025 March 9; published 2025 May 2

Abstract

Titan, Saturn's largest satellite, maintains an atmosphere composed primarily of nitrogen (N_2) and methane (CH_4) that leads to complex organic chemistry. Some of the nitriles (CN-bearing organics) on Titan are known to have substantially enhanced ^{15}N abundances compared to Earth and Titan's dominant nitrogen (N_2) reservoir. The $^{14}N/^{15}N$ isotopic ratio in Titan's nitriles can provide better constraints on the synthesis of nitrogen-bearing organics in planetary atmospheres as well as insights into the origin of Titan's large nitrogen abundance. Using high signal-to-noise ratio (>13), disk-integrated observations obtained with the Atacama Large Millimeter/submillimeter Array Band 6 receiver (211–275 GHz), we measure the $^{14}N/^{15}N$ and $^{12}C/^{13}C$ isotopic ratios of acetonitrile (CH_3CN) in Titan's stratosphere. Using the NEMESIS, we derived the $CH_3CN/^{13}CH_3CN$ ratio to be 89.2 ± 7.0 and the $CH_3CN/CH_3^{13}CN$ ratio to be 91.2 ± 6.0, in agreement with the $^{12}C/^{13}C$ ratio in Titan's methane and other solar system species. We found the $^{14}N/^{15}N$ isotopic ratio to be 68.9 ± 4.2, consistent with previously derived values for HCN and HC_3N, confirming an enhanced ^{15}N abundance in Titan's nitriles compared with the bulk atmospheric N_2 value of $^{14}N/^{15}N = 168$, in agreement with chemical models incorporating isotope-selective photodissociation of N_2 at high altitudes.

Unified Astronomy Thesaurus concepts: Titan (2186); Remote sensing (2191); Radio interferometry (1346); Submillimeter astronomy (1647)

1. Introduction

The origin and evolution of the atmosphere of Titan, Saturn's largest satellite, has been an area of interest for many years. Titan's atmosphere is substantial, with intricate chemistry for a moon, and can provide a template for understanding the compositions of primitive carbon/nitrogen-dominated (exo) planetary atmospheres. As we continue to investigate Titan's atmosphere, more questions arise on topics such as cloud and haze formation, chemical pathways, interactions with surface and subsurface features, and the full extent of Titan's organic inventory (C. Nixon et al. 2018; S. M. MacKenzie et al. 2021). Titan possesses a thick atmosphere composed primarily of molecular nitrogen (N_2) at about 98% and methane (CH_4) at about 2% in the stratosphere, but the origins of these surprisingly abundant gases are not well known. Titan's methane was first observed by G. P. Kuiper (1944), and various ideas have been put forward to explain its presence and persistence (C. A. Nixon et al. 2012), such as diffusion from subsurface reservoirs (K. J. Kossacki & R. D. Lorenz 1996), episodic outgassing from clathrate hydrates (G. Tobie et al. 2006; M. Choukroun et al. 2010), or release from cryolava flows (A. G. Davies et al. 2016).

C. R. Glein (2015) suggested that the gases responsible for forming Titan's dense, nitrogen-rich atmosphere were originally trapped in its core, and that subsequent hydrothermal and cryovolcanic processes were critical to the formation of Titan's atmosphere. However, this is reliant on chemical reactions, outgassing, and transport mechanisms to produce the gas abundances currently observed. C. R. Glein (2015) showed that this method is plausible through mass balance and chemical equilibrium calculations but also acknowledged that missing information, such as a value for a reasonable outgassing efficiency, makes it challenging to conclusively validate the theory. Thus, an external (cometary) source of Titan's nitrogen may be plausible. The isotopic ratios derived for cometary gases are similar to those of Titan's atmosphere, suggesting that the primordial NH_3 reservoir represented by cometary ices could be the source of Titan's nitrogen (K. E. Mandt et al. 2014).

The N_2 and CH_4 in Titan's atmosphere form the basis of a complex chemical reaction network, yet the chemistry involving nitrogen is still not fully constrained (S. M. Hörst 2017; C. A. Nixon 2024). It is particularly important to understand the chemistry of nitriles, as they are the most abundant nitrogen-containing photochemical products and may play a role in prebiotic syntheses (J. Oro et al. 1990), in addition to their importance in the organic chemistry of space and the potential for life beyond Earth in general.

Nitriles often possess a large dipole moment, and thus their rotational transitions can be detected in Titan's atmosphere at

millimeter/submillimeter wavelengths, including HCN, HC_3N, CH_3C_3N, C_2H_5CN, and more (A. Marten et al. 2002; M. Rengel et al. 2011, 2022; M. A. Cordiner et al. 2015; S. M. Hörst 2017; M. Y. Palmer et al. 2017; A. E. Thelen et al. 2020). These molecules, and a diverse population of other organics, are generated in Titan's upper atmosphere through high-altitude photochemistry, following dissociation by UV photons and collisions with charged particles from Saturn's magnetosphere and/or galactic cosmic rays (GCRs).

Previously developed photochemical models (e.g., E. H. Wilson & S. K. Atreya 2004; K. Willacy et al. 2016; M. Dobrijevic & J. Loison 2018; V. Vuitton et al. 2019) obtain a moderately good agreement with the observed abundances of many nitrogen-bearing species in Titan's atmosphere, suggesting good progress in our quantitative understanding of the relevant chemical processes. However, there still exist significant gaps in our knowledge of Titan's photochemistry, in terms of the detailed reaction pathways as a function of altitude. The available photochemical models make different assumptions regarding the relevant reaction pathways, and the $^{14}N/^{15}N$ ratios in Titan's nitriles are particularly sensitive to some of these assumptions. Enrichment (or isotopic fractionation) of ^{15}N relative to Titan's bulk N_2 reservoir is theorized to occur as a result of isotope-selective photodissociation of N_2 (M.-C. Liang et al. 2007), which involves the more efficient self-shielding of $^{14}N_2$ compared with the less abundant $^{14}N^{15}N$ isotopologue at high altitudes, leading to a reservoir of gas-phase atomic nitrogen that is isotopically enriched in ^{15}N. The resulting ^{15}N enrichment is readily passed on to nitrogen-bearing photochemical products. However, the atomic $^{14}N/^{15}N$ ratio is observationally unconstrained and is sensitive to the various model parameters. Incorporation of ^{15}N into nitriles occurs at different rates depending on the altitude-dependent reaction pathways; indeed, the $^{14}N/^{15}N$ isotopic ratio in CH_3CN has been shown to depend on the relative efficiencies of the different formation pathways (M. Dobrijevic & J. Loison 2018), which are not yet fully constrained by experiments. Further studies of the $^{14}N/^{15}N$ ratios in Titan's nitriles are therefore needed to improve our understanding of the relevant chemical processes, which will lead to a better understanding of nitrogen chemistry (including isotope chemistry) in planetary atmospheres.

The first $^{14}N/^{15}N$ isotopic ratio measurement of Titan's atmosphere was by A. Marten et al. (2002), who used the IRAM 30 m telescope to derive a value of $HC^{14}N/HC^{15}N = 60$–70 in the stratosphere. This was followed by M. A. Gurwell (2004) using the Submillimeter Array, who obtained 94 ± 13 and 72 ± 9 depending on the assumed temperature profile. S. Vinatier et al. (2007) subsequently derived $HC^{14}N/HCN^{15}N = 56 \pm 8$ using Cassini infrared spectroscopy. R. Courtin et al. (2011) used the SPIRE instrument on the Herschel spacecraft to derive a ratio of 76 ± 6. The $HC^{14}N/HC^{15}N$ ratio was further refined by E. M. Molter et al. (2016), who obtained 72.2 ± 2.2 using high spectral resolution Atacama Large Millimeter/submillimeter Array (ALMA) observations. Using in situ mass spectrometry, Cassini–Huygens measured the atmospheric $^{14}N_2/^{15}N^{14}N$ ratio, from which a $^{14}N/^{15}N$ ratio of 167.7 ± 0.6 was derived in N_2, which represents the dominant atmospheric nitrogen reservoir (H. B. Niemann et al. 2010).

More recently, M. A. Cordiner et al. (2018) used ALMA to obtain a $^{14}N/^{15}N$ ratio of 67 ± 14 in HC_3N, while M. Y. Palmer et al. (2017) and T. Iino et al. (2020) measured $CH_3C^{14}N/CH_3C^{15}N$ ratios of 89 ± 5 and 125^{+145}_{-44}, respectively.

Table 1
Observed CH_3CN Isotopologue Transitions

Species	Transition[a]	Rest. Freq. (GHz)	E_u (K)
CH_3CN	14_6–13_6	257.3491793	349.7
CH_3CN	14_5–13_5	257.4035843	271.2
CH_3CN	14_4–13_4	257.4481277	206.9
CH_3CN	14_3–13_3	257.4827915	156.9
CH_3CN	14_2–13_2	257.5075614	121.2
CH_3CN	14_1–13_1	257.5224275	99.8
CH_3CN	14_0–13_0	257.5273835	92.7
$CH_3^{13}CN$	14_3–13_3	257.3555752	156.9
$CH_3^{13}CN$	14_2–13_2	257.3802430	121.2
$CH_3^{13}CN$	14_1–13_1	257.3950476	99.8
$CH_3^{13}CN$	14_0–13_0	257.3999832	92.6
$CH_3C^{15}N$	15_5–14_5	267.4868839	281.6
$CH_3C^{15}N$	15_4–14_4	267.5323198	217.2
$CH_3C^{15}N$	15_3–14_3	267.5676777	167.1
$CH_3C^{15}N$	15_2–14_2	267.5929435	131.3
$CH_3C^{15}N$	15_1–14_1	267.6081070	109.9
$CH_3C^{15}N$	15_0–14_0	267.6131621	102.7
$^{13}CH_3CN$	15_5–14_5	267.8245852	281.7
$^{13}CH_3CN$	15_4–14_4	267.8698337	217.3
$^{13}CH_3CN$	15_3–14_3	267.9050464	167.2
$^{13}CH_3CN$	15_2–14_2	267.9302086	131.5
$^{13}CH_3CN$	15_1–14_1	267.9453102	110.0
$^{13}CH_3CN$	15_0–14_0	267.9503447	102.8

Note.
[a] Rotational transitions are denoted as $J'_{K'} - J''_{K''}$, where the transition is from the upper state to the lower state and K represents the angular momentum quantum number.

While there is some apparent scatter among the various measurements, a significant difference is evident between the ^{15}N fractions in the (trace) photochemical products and the (bulk) nitrogen (N_2) reservoir, which can be explained as a result of isotope-selective N_2 photodissociation by solar radiation (M.-C. Liang et al. 2007; V. Vuitton et al. 2019). The significance of any differences in the degree of ^{15}N enrichment among different nitriles is yet to be investigated in detail. As one of the most abundant nitriles in Titan's atmosphere, more accurate measurements of the CH_3CN isotopologues, in particular, are justified to help test and improve models for Titan's nitrogen chemistry.

2. Observations

To investigate Titan's high-altitude nitrogen chemistry, we obtained observations using the ALMA Band 6 receiver (211–275 GHz; ~1.1–1.4 mm) in 2019 as part of project #2019.1.00783.S. Three spectral settings were observed (see A. E. Thelen et al. 2020 for details), the first of which (Science Goal 1; SG1) covered the CO $J = 2$–1 line, and the remaining two (SGs 2 and 3) covered observations of multiple nitrile species and their carbon and nitrogen isotopes. The data from SGs 2 and 3 used in the present study were observed in several nonconsecutive frequency intervals between 256.9–257.8 GHz and 267.0–268.9 GHz (see Table 1).

As described by A. E. Thelen et al. (2020), the data were taken during multiple execution blocks between 2019 November 14 and December 16 using ALMA configurations C43-1,

C43-2 (maximum baselines ranging from 160 to 314 m), and C43-3 (maximum baselines of 500 m). The resulting beam size was $1\farcs54 \times 1\farcs14$ in the 256–257 GHz range and $1\farcs56 \times 1\farcs11$ in the 267–268 GHz range, so Titan ($\approx 1\farcs0$ diameter on the sky, including its solid disk and extended atmosphere) was not resolved, enabling the maximum sensitivity per beam for disk-averaged studies of Titan's entire Earth-facing atmosphere. The spectral resolution of the CH_3CN and $CH_3^{13}CN$ isotopologues was 488 kHz, and the resolution for the $^{13}CH_3CN$ and $CH_3C^{15}N$ isotopologues was 976 kHz. The data were processed and calibrated using version 5.6.1-8 of the CASA pipeline using standard scripts provided by the Joint ALMA Observatory (JAO). Additional bandpass calibration smoothing was performed to improve the spectral noise per channel, and the tclean procedure was used to reconstruct the sky model. For a more complete description of the observations and data processing, we refer the reader to A. E. Thelen et al. (2020).

A list of the observed CH_3CN spectral lines of relevance to the present study, as well as their frequencies and upper-state energies (E_u), are shown in Table 1. The total signal-to-noise ratios (SNRs) integrated across the full width of all detected CH_3CN lines are 1450 for the major isotopologue, 13 for $^{13}CH_3CN$, 15 for $CH_3^{13}CN$, and 16 for $CH_3C^{15}N$.

3. Radiative Transfer Modeling

From the processed data cubes, disk-averaged spectra were extracted using a circular aperture with a radius of $1\farcs8$, which includes Titan up to the top of its atmosphere plus half a beam to account for all emission. Titan's disk was divided into 35 annuli corresponding to different emission angles from 3° to 75° covering the center of Titan up to a tangential altitude of 1200 km (N. Teanby et al. 2013), the vertical extent of our model. Spectral models were generated using the line-by-line module of the Nonlinear optimal Estimator for MultivariatE spectral analySIS (NEMESIS) radiative transfer and retrieval tool (P. Irwin et al. 2008). NEMESIS applies an iterative minimization technique to the cost function (including the goodness of fit, χ^2, combined with the a priori errors) in order to obtain an optimized spectral model, temperature and abundance profiles as a function of altitude. NEMESIS includes the necessary physical parameters such as spontaneous emission and absorption of radiation, on- and off-limb emission angles, continuum opacity and thermal and pressure broadening, as well as temperature dependence when computing model fluxes as a function of wavelength. This allows a full characterization of the observed spectral line profiles, leading to robust abundance measurements.

To further improve the accuracy of our model retrieval results, updates were made to the spectral line database and instrumental broadening function. The NEMESIS line database was updated to the GEISA 211 format (N. Jacquinet-Husson et al. 2005) for additional precision on the rest frequencies and intensities. We initially used the line data from the Cologne Database for Molecular Spectroscopy (CDMS; H. S. P. Müller et al. 2001) but found discrepancies in the line intensities and partition function coefficients for the major isotopologue and ^{13}C minor isotopologues. These values were not sufficiently accurate in this frequency range; therefore, all of the values were recomputed without hyperfine or vibrational corrections in a self-consistent manner. Note that the hyperfine splittings for all relevant transitions are much smaller than the resolution of our observed spectra. We refer the reader to Appendix A for more details. The partition functions for all of the isotopologues were tabulated for inclusion in NEMESIS using a third-order polynomial fit to the recomputed values listed in Table 2. We also updated the instrumental line shape used by NEMESIS to account for the intrinsic (non-Gaussian) shape of the ALMA line-spread function, as well as including the potential effects of Doppler broadening of the lines due to Titan's zonal winds (see Appendix B for details).

Table 2
Partition Functions for CH_3CN Isotopologues as a Function of Temperature

T (K)	Q (CH_3CN)	Q ($^{13}CH_3CN$)	Q ($CH_3^{13}CN$)	Q ($CH_3C^{15}N$)
300.0	10118.2635	10418.8811	10123.2613	10431.9556
225.0	6570.5621	6765.7543	6573.8080	6774.2565
150.0	3576.3518	3682.5661	3578.1185	3687.1996
75.00	1265.1853	1302.7260	1265.8098	1304.3662
37.50	449.0803	462.3803	449.3016	462.9618
18.75	164.3168	169.1645	164.3975	169.3765
9.375	64.0955	65.9716	64.1267	66.0537

Optimization of the vertical abundance profile began with a reasonable guess based on prior measurements. For the major CH_3CN isotopologue, we used an a priori profile based on the disk-averaged measurements from A. Marten et al. (2002) up to 500 km, supplemented by data from the model of J. Loison et al. (2015) up to 1200 km. The error on this "a priori" profile was set to a constant value of 100%. From the N_2 broadening parameters of CH_3CN calculated by A. Dudaryonok et al. (2015), we assumed an average value for the Lorentzian half-width using the $K = 0$ and $K = 5$, J = 14–13 coefficients ($\Gamma = 0.158\ \mathrm{cm^{-1}\ atm^{-1}}$) and temperature exponent ($\alpha = 0.60$). The collision-induced absorption parameters used include all combinations of N_2, CH_4, and H_2 and are calculated by following the routines of A. Borysow & L. Frommhold (1986a, 1986b, 1986c, 1987) and A. Borysow & C. Tang (1993). The atmospheric temperature vertical profile was obtained by modeling the ALMA CO data obtained contemporaneously with our observations (see A. E. Thelen et al. 2020 for details). A correlation length of 3.0 atmospheric scale heights was used to internally smooth the optimized vertical profiles. The observed ALMA flux spectra were scaled by a constant factor (≈ 1.02) to produce a match between the modeled and observed continuum levels. This scaling mitigates errors on the ALMA flux scale (which may be as much as $\approx 10\%$, due to uncertainty in the amplitude calibrator flux), as well as accounting for small errors in the assumed (a priori) temperature around the tropopause, which determines the model continuum level. The CH_3CN major isotopologue profile was continuously retrieved at each altitude to obtain an optimized fit to the observed spectral line profiles. The retrieved profile was found to be consistent across several forms of a priori profiles (see Appendix E) as shown in Figure 9.

The minor CH_3CN isotopologue spectra are noisier and contain less vertical information than the major isotopologue, so we used the best-fitting CH_3CN main isotopologue abundance profile scaled by a uniform factor, which was varied to obtain the best fit for those species. The results of an attempted, continuously variable $CH_3C^{15}N$ retrieval are discussed in Appendix C.

Finally, we tested the sensitivity of our retrieved isotopic ratios to uncertainties in the atmospheric temperature profile

(A. E. Thelen et al. 2020), which vary between 1 and 5 K as a function of altitude. Due to the close similarities in the observed frequencies and energy levels of the different isotopologues, their line strengths scale similarly with temperature, so these uncertainties only amount to an additional error of <0.8% on the retrieved isotopic ratios.

4. Results

Our CH_3CN spectral fits and retrieved vertical abundance and temperature profiles are shown in Figure 1. We derived scaling factors representative of the mean isotopic ratios over Titan's disk-averaged atmosphere for the three minor CH_3CN isotopologues, including the ^{15}N isotopologue and both ^{13}C isotopologues. The $CH_3CN/CH_3C^{15}N$ isotopic ratio was derived to be 68.9 ± 4.2, the $CH_3CN/^{13}CH_3CN$ ratio was derived to be 89.2 ± 7.0, and the $CH_3CN/CH_3^{13}CN$ ratio was derived to be 91.2 ± 6.0. Our derived $^{14}N/^{15}N$ isotopic ratio for the major isotopologue is shown for comparison with previously obtained ratios for HCN, HC_3N, and CH_3CN as well as N_2 in Figure 2.

Within the noise, our spectral models provide an excellent fit to the observed Titan continuum, line cores, and line wings. In the lower stratosphere (below 150 km altitude), our retrieved CH_3CN vertical abundance (volume mixing ratio (VMR)) profile closely matches the steepness of the A. Marten et al. (2002) a priori. Our retrieved abundances drop somewhat below the a priori in the mid-to-upper stratosphere, with the notable exception of a maximum around 250 km, although there may be some doubt as to the physical origin of this relatively narrow feature, since it is not present in the ALMA profile retrieved by E. Lellouch et al. (2019) or the photochemical model results of M. Dobrijevic & J. Loison (2018) and V. Vuitton et al. (2019). Considering our observations are averaged over Titan's entire Earth-facing hemisphere, the resulting spectra represent a weighted average across all latitudes and altitudes. It therefore cannot be determined where exactly (latitudinally) in Titan's atmosphere this peak originates. On the other hand, this feature is found to be necessary to obtain a good fit to the observed spectra—otherwise, the line core and wing strengths cannot be simultaneously reproduced.

Based on the CH_3CN maps previously published by M. A. Cordiner et al. (2019) and A. E. Thelen et al. (2019, 2024), CH_3CN is most concentrated around Titan's poles. The stratospheric CH_3CN enhancement could be consistent with the presence of unresolved abundance peak(s) within the beam associated with one or both of these regions. It can be speculated that the contribution is potentially coming from the trapping of molecules and subsidence in the (cold) polar regions, possibly at different altitudes around the north and south poles (see N. A. Teanby et al. 2008, 2017, 2019, for example).

We then used the contribution functions from our best-fitting radiative transfer models to calculate weighted mean emission altitudes, which represent the average altitude to which our results are sensitive. These were determined to be ∼230 km for $^{13}CH_3CN$ and $CH_3C^{15}N$ (and ∼246 km for the major isotopologue).

To make a detailed comparison with the $CH_3CN/CH_3C^{15}N$ vertical profiles produced by photochemical models, we also performed a continuously variable $CH_3C^{15}N$ VMR fit. However, the spectroscopic SNR of 16 was found to be insufficient to provide useful constraints on the $^{14}N/^{15}N$ ratio as a function of altitude (see Appendix C).

5. Discussion

We now compare our isotopic ratios to those previously obtained in the Titan literature. We find that our $CH_3CN/CH_3C^{15}N$ ratio of 68.9 ± 4.2 is significantly lower than the $^{14}N/^{15}N$ ratio in N_2 of 167.7 ± 0.6 obtained by Cassini mass spectrometry (H. B. Niemann et al. 2010), indicating strong ^{15}N enrichment in Titan's CH_3CN. On the other hand, our result is within 1.6σ of the previous Cassini CIRS measurement for HCN (56 ± 8; S. Vinatier et al. 2007). Additionally, our ratio is within 1σ of the A. Marten et al. (2002) HCN value of 60–70, about 2σ of both derived $^{14}N/^{15}N$ ratios in HCN of 94 ± 13 and 108 ± 20 from M. A. Gurwell (2004), and is within 1.2σ of the R. Courtin et al. (2011) ratio of 76 ± 6. The HCN measurement using ALMA of 72.2 ± 2.2 by E. M. Molter et al. (2016) is also within 1σ of our derived ratio. Within the errors, our result is also consistent with the $^{14}N/^{15}N$ ratio in HC_3N (67 ± 14; M. A. Cordiner et al. 2018) and within 1.3σ of the previous best value for the $CH_3CN/CH_3C^{15}N$ ratio of 125^{+145}_{-44}, obtained using ALMA archival flux calibration data by T. Iino et al. (2020). Although the apparent difference between our value and that of T. Iino et al. (2020) could be explained solely as a result of statistical noise, it should be noted that our improved values for the spectral line intensities and partition functions compared with those in CDMS (see Appendix A) resulted in a downward revision of the $^{14}N/^{15}N$ ratio by ∼18%, ∼23% for $CH_3CN/^{13}CH_3CN$, and ∼34% for $CH_3CN/CH_3^{13}CN$, so this could explain some of the discrepancy.

Overall, our derived ratio is in relatively good agreement with the previously obtained nitrogen isotopic ratios, with the exception of N_2. By far the dominant form of nitrogen in Titan's atmosphere is N_2, so we take the $^{14}N/^{15}N$ ratio in N_2 to be representative of Titan's intrinsic isotopic composition. Isotope-selective photodissociation of N_2 in the upper atmosphere provides a reservoir of ^{15}N-enriched atomic nitrogen that feeds into the altitude-dependent nitrogen chemistry, resulting in the synthesis of ^{15}N-enriched nitriles such as CH_3CN. In Figure 57 of V. Vuitton et al. (2019), the peak density for atomic ^{14}N and ^{15}N occurs in Titan's thermosphere between 1100 and 1200 km, falling rapidly below ∼700 km. However, the atomic $^{14}N/^{15}N$ isotopic ratio reaches a peak value of ∼25 at ∼900 km, below the point of the peak atomic ^{14}N and ^{15}N values. There are approximately constant values for the wings of the distribution of the $^{14}N/^{15}N$ ratio: ∼85 at ∼1200 km and above and ∼100 at ∼800 km and below. Thus, the incorporation of fractionated nitrogen, and therefore production of nitriles, occurs primarily above ∼700 km in the V. Vuitton et al. (2019) model, followed by downward mixing and diffusion toward the stratosphere, into the region between 150 and 300 km, to which our ALMA observations are most sensitive. The enriched ^{15}N abundance in the main nitrile production thus leads to a decrease in the $^{14}N/^{15}N$ isotopic ratio for CH_3CN. The large difference between the isotopic ratios in N_2 and CH_3CN is consistent with this picture. Also comparing the $^{14}N/^{15}N$ ratio profiles for HCN, CH_3CN, and HC_3N shown in Figure 58 of V. Vuitton et al. (2019) reveals that they should be expected to follow a similar general trend, with decreased values at altitudes below ∼800 km.

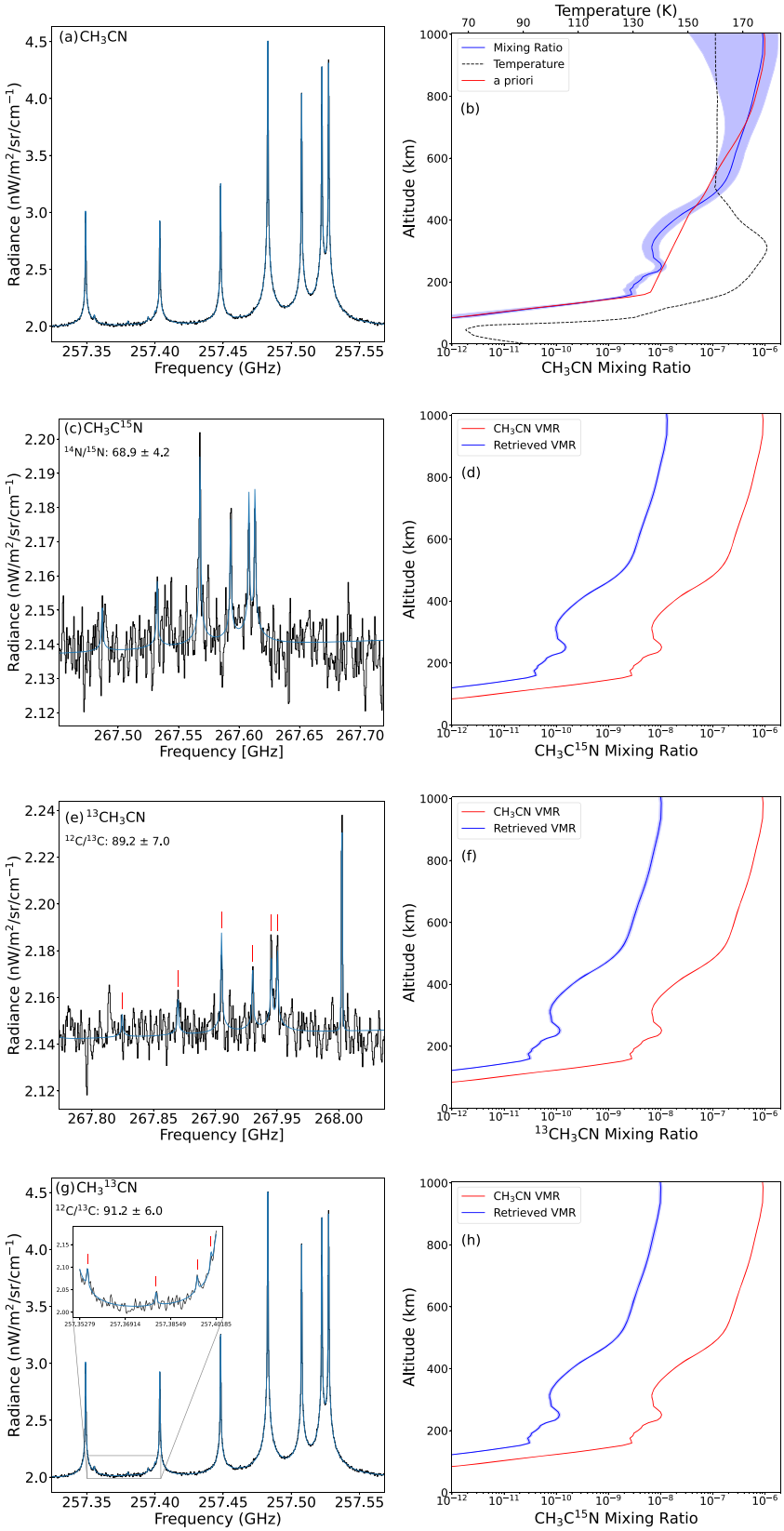

Figure 1. Optimized model fits for all isotopologues in the left column, panels (a), (c), (e), and (g). The data are in black, and the model is in blue. The molecule is identified in the top left corner of the panel along with the corresponding scaling factor. The respective retrieved vertical profiles (VMRs) are in the right column, panels (b), (d), (f), and (h). In all profiles, the red line is the a priori profile, the blue line is the retrieved VMR profile, and the shaded region is the error on the retrieved VMR profile. For the major isotopologue, the dashed black line in panel (b) is the temperature profile. The error envelope of the minor isotopologues is quite narrow; it is within 6%–8% of the obtained isotope ratio value. The red ticks in (e) and (g) identify the $^{13}CH_3CN$ and $CH_3^{13}CN$ lines, respectively, in the data. The highest-frequency line in (e) is the $J = 30$–29, $K_a = 3$ transition of C_2H_5CN (propionitrile; ethyl cyanide) at 268.0025 GHz.

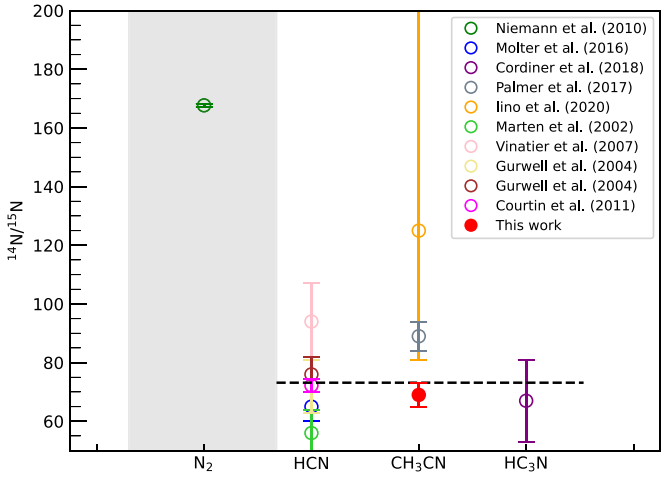

Figure 2. Derived $^{14}N/^{15}N$ isotopic ratios for molecules in Titan's atmosphere, including the value derived in this work in red. The N_2 data point is plotted against a gray background to distinguish it as the main atmospheric nitrogen reservoir. The black dashed line is the error-weighted average of previously measured $^{14}N/^{15}N$ ratios from A. Marten et al. (2002), M. A. Gurwell (2004), S. Vinatier et al. (2007), R. Courtin et al. (2011), E. M. Molter et al. (2016), M. A. Cordiner et al. (2018), and T. Iino et al. (2020).

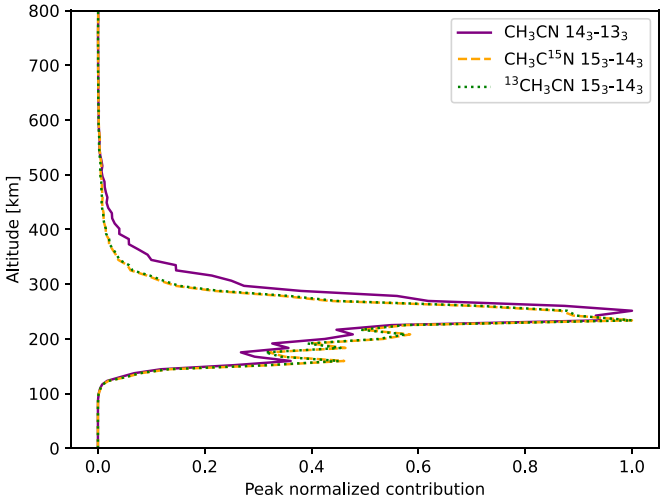

Figure 3. Contribution functions for the strongest lines ($K = 3$) of CH_3CN and its minor isotopologues.

Isotopic ratios for $^{12}C/^{13}C$ have previously been measured on Titan for CH_4 (H. B. Niemann et al. 2010), CH_3D (B. Bézard et al. 2007), CO_2 (C. A. Nixon et al. 2008b), CO (R. Courtin et al. 2011; M. Rengel et al. 2014; J. Serigano et al. 2016), C_4H_2 (A. Jolly et al. 2010), C_2H_2 (C. Nixon et al. 2008a), C_2H_6 (C. Nixon et al. 2008a), HC_3N (D. E. Jennings et al. 2008), and HCN (T. Hidayat et al. 1997; R. Courtin et al. 2011; M. Rengel et al. 2014; E. M. Molter et al. 2016). Comparing the error-weighted mean isotopic ratio for these molecules, 89.8 ± 6.9, to our derived $^{12}C/^{13}C$ ratios in CH_3CN of 89.2 ± 7.0 and 91.2 ± 6.0, we find that they are all consistently within a 1σ error margin. The observed $^{12}C/^{13}C$ ratios are therefore consistent with the dominant carbon reservoir in Titan's atmosphere (H. B. Niemann et al. 2010; K. E. Mandt et al. 2012; C. A. Nixon et al. 2012)—as expected considering a lack of strong isotopic fractionation mechanisms involving carbon at the altitudes we observed. Unlike N_2, CH_4 is not subject to isotope-selective self-shielding, so variable $^{12}C/^{13}C$ ratios among the different CH_3CN carbon atoms (as well as other molecules) are not expected. Additionally, when comparing our derived $^{12}C/^{13}C$ ratios to the error-weighted mean for comets (88.6 ± 6.5, which excludes the outlier for H_2CO in comet 67P; K. Altwegg et al. 2020), and with the terrestrial value of 89.0, we also find that our measurements are within 1σ. Thus, our $^{12}C/^{13}C$ ratios are in good agreement with the values previously derived for Titan and various other solar system bodies, including other bodies within the Saturnian system (see H. Nomura et al. 2022 and references therein). We thus confirm the trend for a lower degree of isotopic fractionation in carbon than for nitrogen across various solar system bodies.

The improved accuracy of our $CH_3CN/CH_3C^{15}N$ ratio compared with T. Iino et al. (2020) leads to new constraints on models for the CH_3CN production pathways and nitrogen fractionation processes in Titan's atmosphere. The model by V. Vuitton et al. (2019) includes multiple pathways to CH_3CN, the most important being

$$H + CH_2CN \xrightarrow{M} CH_3CN, \quad (1)$$

$$N(^2D) + C_2H_4 \longrightarrow CH_3CN + H, \quad (2)$$

and

$$HCNH^+ + CH_3 \longrightarrow CH_3CNH^+ + H, \quad (3)$$

followed by

$$CH_3CNH^+ + e^- \longrightarrow CH_3CN + H. \quad (4)$$

N. Balucani et al. (2012) showed that Equation (2) is inefficient since it favors the alternative isomeric product forms—CH_2NCH and c-$CH_2(N)CH$—rather than CH_3CN. M. Dobrijevic & J. Loison (2018) suggested that Equation (1) may not be the dominant route to CH_3CN since it primarily occurs at the higher pressures found in the lower atmosphere.

If Reaction (3) (followed by Reaction (4)) is the primary route to CH_3CN (and therefore $CH_3C^{15}N$ via $HC^{15}NH^+$), then this could help explain the similarity between the observed $^{14}N/^{15}N$ isotopic ratios in HCN and CH_3CN.

We now compare our derived scaled nitrogen isotopic ratio with the models of M. Dobrijevic & J. Loison (2018) and V. Vuitton et al. (2019) to gain better insight into how ^{15}N may be incorporated into CH_3CN. At the value of our peak observed altitudinal sensitivity (≈230 km), our value of $^{14}N/^{15}N = 69 \pm 4$ is in better agreement with the V. Vuitton et al. (2019) model value of ∼55 than the M. Dobrijevic & J. Loison (2018) model value of ∼120 (with GCRs included; see Figure 4). On the other hand, our observed $CH_3CN/CH_3C^{15}N$ ratio is a closer match with the M. Dobrijevic & J. Loison (2018) model without GCRs included. However, cosmic rays are known to play a significant role in the photochemistry and ionization, primarily of Titan's lower stratosphere and troposphere (C. A. Nixon 2024), so it is unclear whether this is a useful comparison. Nevertheless, it may indicate that cosmic ray chemistry should not be considered as a strong factor influencing the stratospheric $CH_3CN/CH_3C^{15}N$ ratio.

The importance of magnetospheric electrons is another difference between the M. Dobrijevic & J. Loison (2018) and V. Vuitton et al. (2019) models. In the M. Dobrijevic & J. Loison (2018) model, dissociation of N_2 by magnetospheric electrons provides an additional source of atomic nitrogen not included in the V. Vuitton et al. (2019) model, particularly important in the upper atmosphere (at altitudes of 700–1200 km). Since electron-impact dissociation of N_2 is not isotope-selective, the resulting

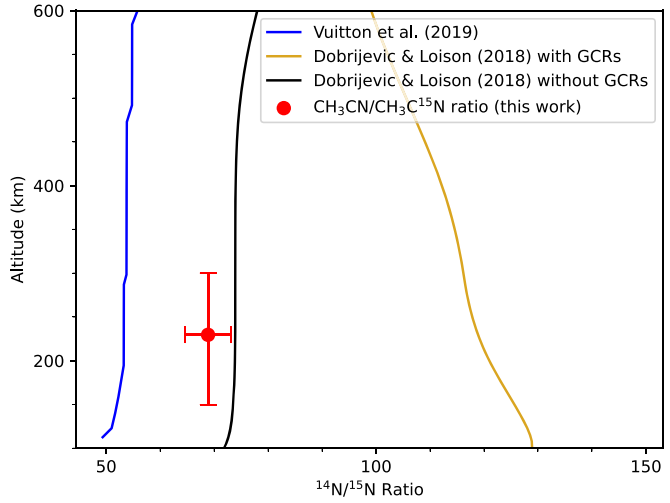

Figure 4. $CH_3CN/CH_3C^{15}N$ isotopic ratio (red point) derived from our scale-factor retrieval, with the horizontal error bar showing the error on the ratio value and the vertical bar spanning the region of highest sensitivity: 150–300 km. For comparison, the chemical model results of M. Dobrijevic & J. Loison (2018; black, without cosmic rays; gold, with cosmic rays) and V. Vuitton et al. (2019; blue line) are shown.

additional source of atomic nitrogen in this altitude range has a $^{14}N/^{15}N$ ratio equal to that of N_2. This causes the total atomic $^{14}N/^{15}N$ ratio to tend toward larger values, with a corresponding impact on the $^{14}N/^{15}N$ ratio for nitriles produced in this region. The fact that our derived isotopic ratio is greater than that of the V. Vuitton et al. (2019) model but less than that of the M. Dobrijevic & J. Loison (2018) model (without GCRs) would suggest that magentospheric electrons could be important as a minor source of atomic ^{15}N.

While our derived isotopic ratios are in good agreement with previous measurements on Titan (S. M. Hörst 2017), it is of interest to compare with other solar system bodies. Based on the data collated by H. Nomura et al. (2022 and references therein), we identify some general trends for the $^{12}C/^{13}C$ and $^{14}N/^{15}N$ isotopic ratios. The carbon ratios are shown to have only small variations from planet to planet, and most of the error bars are fairly well constrained. However, some measurements do have errors too large to constrain the exact variations. Most of the measurements for comets also maintain small variations, with the exception of the value of 40 ± 14 (K. Altwegg et al. 2020) for H_2CO in comet 67P, while some have large error bars that are also unable to completely constrain the variations. Meteorites have a larger range of variation. In contrast, the nitrogen isotopic ratios are shown to generally vary among the objects in the solar system and may have some smaller variations among ratios of the same object depending on the molecule of interest.

Given the results of our study, we can speculate about the origin of Titan's dense nitrogen reservoir. In future studies, it would be useful to gain more insight into the the amount of N_2 that Titan has lost since it formed; the present-day isotopic ratios of heavy noble gases would also be useful in this regard. This could help determine if Titan's N_2 was formed internally through hydrothermal and cryovolcanic processes and/or if the N_2 was formed through photochemical reactions involving accreted cometary ices. All the nitriles observed to date show a strong ^{15}N enrichment. As they mix downward, these nitriles condense into aerosols and precipitate onto the surface, so over time, some of the ^{15}N is removed from the atmosphere. Therefore, the overall atmospheric $^{14}N/^{15}N$ ratio should increase over time, suggesting that Titan's atmospheric nitrogen could have been more ^{15}N-rich in the past—possibly more similar to the value of ≈144 found in comets (H. Nomura et al. 2022). To confirm this hypothesis will require continued, high-accuracy studies of $^{14}N/^{15}N$ ratios in cometary nitrogen-bearing species (N_2, NH_3, HCN, and other organics), as well as in the various nitrogen-bearing compounds found in Titan's surface and atmosphere.

6. Conclusions

Using high-SNR (13–1450) ALMA observations from 2019, we derived the first well-constrained isotopologue abundance ratios for CH_3CN in Titan's atmosphere: 68.9 ± 4.2 for $CH_3CN/CH_3C^{15}N$, 89.2 ± 7.0 for $CH_3CN/^{13}CH_3CN$, and 91.2 ± 6.0 for $CH_3CN/CH_3^{13}CN$. These ratios represent disk-averaged values but are most sensitive to gases in the altitude range 150–300 km, with a peak sensitivity around 230 km. We therefore show for the first time that ^{15}N is strongly enhanced in CH_3CN compared to Titan's main atmospheric nitrogen reservoir (N_2). This can be explained as a result of photochemical isotopic fractionation initiated by isotope-selective photodissociation of N_2 in the thermosphere. We find a consistent level of ^{15}N enrichment within all of Titan's nitriles measured to date, which implies that they likely formed from a common, isotopically fractionated reservoir of atmospheric nitrogen. Loss of atmospheric ^{15}N due to isotopic fractionation into nitriles should therefore be considered as a potentially important isotope sink in future studies of the time evolution of Titan's atmospheric $^{14}N/^{15}N$ ratio, with implications for our understanding of the origins of Titan's nitrogen reservoir. Comparison between our observed nitrogen isotopic ratio and the results from previous photochemical models shows better agreement with the V. Vuitton et al. (2019) model than the M. Dobrijevic & J. Loison (2018) model that includes N_2 dissociation by cosmic rays and mesospheric electrons, but there is still room for improvement, so the precise importance of these processes should be revisited in future modeling efforts. Future observations at higher SNR (by at least a factor of 5 for the minor isotopologue) will be required to investigate variability in the nitrile $^{14}N/^{15}N$ ratios as a function of altitude.

Acknowledgments

This paper makes use of the following ALMA data: ADS/JAO.ALMA#2019.1.00783.S. ALMA is a partnership of ESO (representing its member states), NSF (USA) and NINS (JAPAN), together with NRC (Canada), NSTC and ASIAA (Taiwan), and KASI (republic of Korea), in cooperation with the Republic of Chile. The Joint ALMA Observatory is operated by ESO, AUI/NRAO, and NAOJ.

The work done by M.A.C., A.E.T., and C.A.N. was funded by NASA's Solar System Observation (SSO) Program. J.N. was funded by the ALMA SOS program, and N.A.T. was funded by STFC grant ST/Y000676/1.

Appendix A
CH_3CN Spectroscopic Parameters and Partition Functions

We used frequency predictions of acetonitrile (methyl cyanide; CH_3CN) taken from CDMS (H. S. P. Müller et al. 2001) and noticed that the current CDMS predictions (H. S. P. Müller et al. 2009) for the ground state were based

on data with a significant missing window in experimental coverage around 257 GHz of current detections. The nearest experimental measurements were for the $J = 8$–7 transition near 147 GHz (D. Boucher et al. 1977) and then the $J = 18$–17 transition near 331 GHz (G. Cazzoli & C. Puzzarini 2006). For this reason, we carried out an experimental double check of the prediction accuracy in this missing window by measuring $K = 0$–9 transitions for $J = 14$–13 at 257 GHz and $J = 15$–14 at 275 GHz. Measurements were made at room temperature and at around 1 mTorr sample pressure by using the broadband millimeter-wave spectrometer in Warsaw (I. Medvedev et al. 2004). This verification turned out to be positive since CDMS predictions and currently measured frequencies for 20 different transitions were in agreement to a rms deviation of 16 kHz, which is well within the nominal uncertainty of the employed spectrometer.

Another issue that we faced in deriving the isotopic ratios was the need for a unified partition function for the parent species and its ^{13}C isotopic variants. The values in the ground-state entry in CDMS also accounted for the levels in the $v_8 = 1$ excited vibrational state, while those for the ^{13}C species did not. For this reason, we reevaluated the partition function for the ground state of the parent at the same conditions as for the isotopic species, namely, without the $v_8 = 1$ state and without accounting for the nitrogen hyperfine structure (Table 2), which is unresolved at the resolution of our data. Omission of the CH_3CN vibrationally excited state amounts to a 7% underestimation of the partition function. As a result of these improvements to the line intensities and partition functions, we found that the retrieved isotopic ratios decreased by 20% for the $^{14}N/^{15}N$ ratio, 23% for the $CH_3CN/^{13}CH_3CN$ ratio, and 27% for the $CH_3CN/CH_3^{13}CN$ ratio.

Appendix B
Line-shape Function

In order to account for the potential effects of rotational broadening of the lines in the data, we generated a new instrumental line-spread function for inclusion in NEMESIS. A rotationally broadened spectral profile was created using a modified version of the code published in M. A. Cordiner et al. (2020), including the impact of Titan's winds on the CH_3CN Doppler line profile based on the observed wind field in 2017 May. We convolved the rotationally broadened profile with a line-shape function that mimics the ALMA correlator response, which is the Fourier transform of a (padded) Hann window, to get the new line-spread function (R. Hills 2016; Figure 5). Note that the amount of padding used sets the frequency domain sampling, and we set this to correspond to two channels, according to the standard setup of the ALMA correlator. Our observations were obtained at two different spectral resolutions (488 and 976 kHz), corresponding to a velocity FWHM of 568 and 1090 m s^{-1} at 257.4461 and 267.5854 GHz, respectively. After the addition of wind broadening, the 488 kHz velocity FWHM increased to 604 m s^{-1} (a difference of 36 m s^{-1}), and the 976 kHz velocity FWHM increased to 1109 m s^{-1} (a difference of 19 m s^{-1}), so the line-shape function had a slight impact on the results.

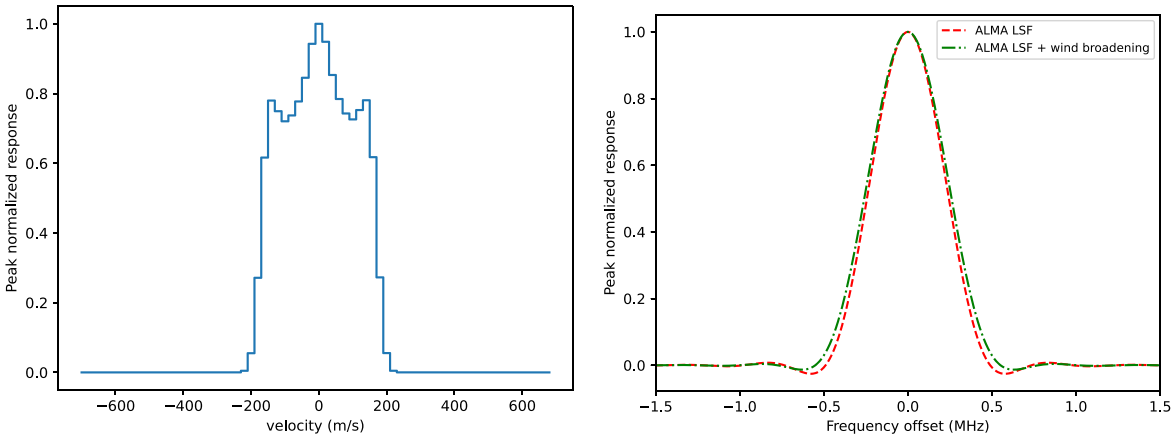

Figure 5. Spectral line broadening profile based on the CH_3CN wind field observed by M. A. Cordiner et al. (2020; left) and the final line-spread function with wind-induced broadening as well as the Hanning-smoothed sinc response of the ALMA correlator (right).

Appendix C
Continuous $^{14}N/^{15}N$ Profile Retrieval

To investigate the vertical behavior of the $CH_3CN/CH_3C^{15}N$ ratio, we used NEMESIS to perform a continuously variable abundance profile retrieval for $CH_3C^{15}N$, the result of which is shown in Figure 6. The resulting $^{14}N/^{15}N$ ratio and error envelope are shown in Figure 7, where the errors represent the actual retrieval error, accounting for both the model and (lack of) a priori errors. Since these errors are so large, there is no strong evidence for variability in the $^{14}N/^{15}N$ ratio with altitude based on our ALMA data.

As discussed in Section 5, the two photochemical models make different assumptions about reaction pathways, including the weight given to interactions with magnetospheric electrons and cosmic rays, so further investigations of the $^{14}N/^{15}N$ ratio as a function of altitude would be useful to help distinguish between the differing altitudinal dependencies as well as the impacts on the chemistry, as this will affect the abundance (and thus isotope) profiles differently at different altitudes.

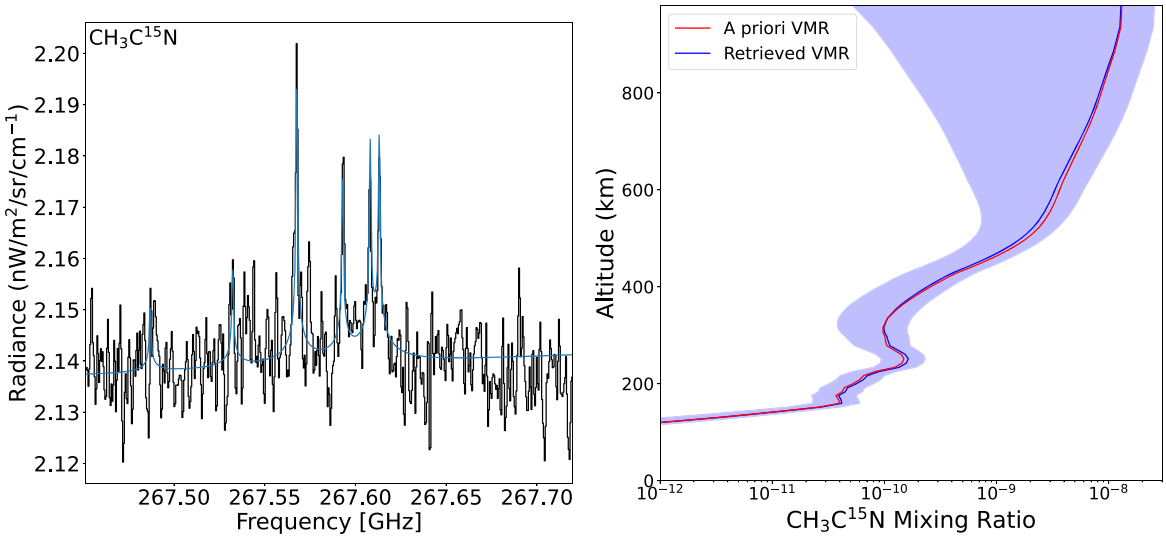

Figure 6. Continuously retrieved $CH_3C^{15}N$ model fit (left) and VMR profile (right). As in Figures 1(a) and 1(b), the data are in black, and the model is in blue; in the right panel, the red line is the a priori profile, the blue line is the retrieved VMR profile, and the shaded region is the error on the retrieved VMR profile.

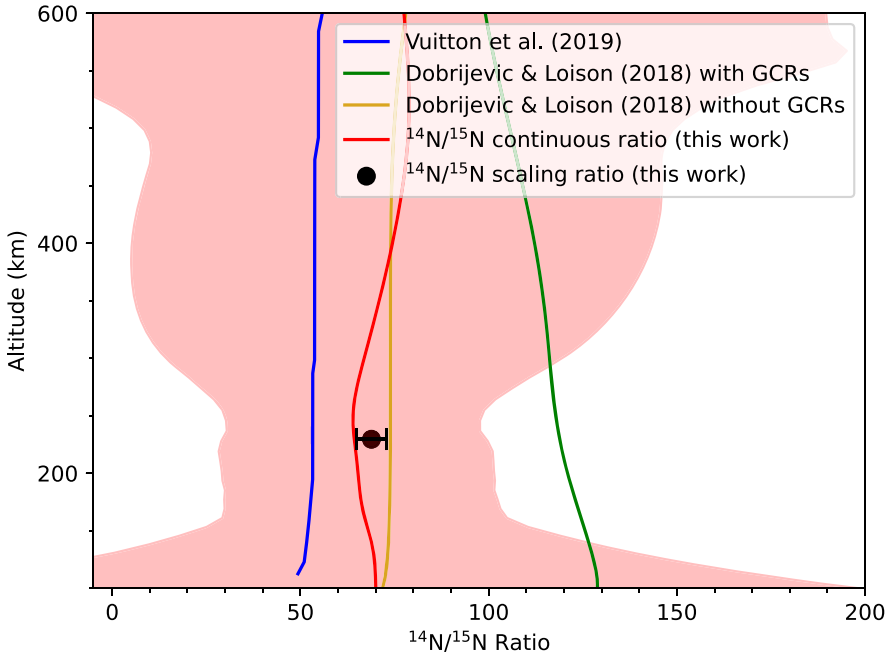

Figure 7. Derived continuous $CH_3CN/CH_3C^{15}N$ isotopic ratio profile with error envelope (red; shaded red region) plotted with photochemical model profiles from M. Dobrijevic & J. Loison (2018; green and gold) and V. Vuitton et al. (2019; blue). The black point is our measured scaling factor for the $CH_3CN/CH_3C^{15}N$ isotopic ratio from this work, plotted at the weighted mean emission altitude of 230 km (with its corresponding error bars).

Appendix D
Averaging Kernels

The averaging kernels for an atmospheric abundance retrieval are the product of the gain matrix (G) and Jacobian matrix (J) and provide a representation of the correlation between the retrieved abundance of each atmospheric level with respect to the other levels. Averaging kernels for our best-fitting CH_3CN NEMESIS model are shown in Figure 8. The averaging kernels can be used in tandem with the contribution functions to gain a better understanding of the origin of the spectral line emission and the sensitivity of the model. The altitudes with the largest kernel values (which also have the narrowest vertical envelopes) represent the region of the atmosphere to which our retrieved abundances are most sensitive and with the highest altitudinal resolution—i.e., in the range ∼150–300 km. For more details on the formal definitions of G, J, and the averaging kernel, see C. D. Rodgers (1976).

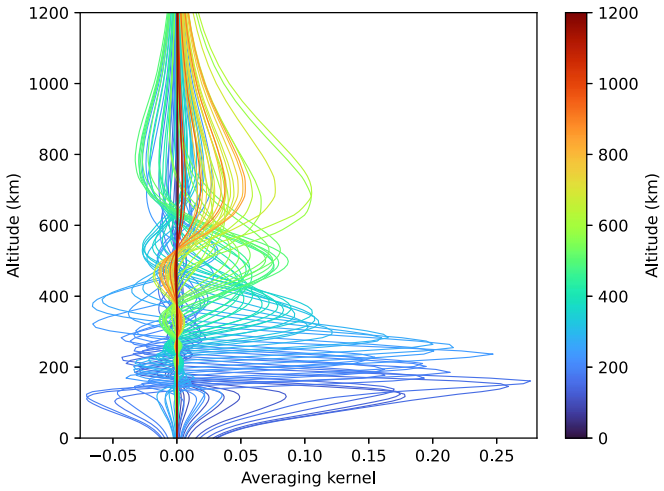

Figure 8. Averaging kernels for the CH_3CN major isotopologue, from our best-fitting NEMESIS model. The color bar shows the representative altitude applicable for each kernel. The altitudes with the largest values (∼150–300 km) indicate the region of highest sensitivity of our model.

Appendix E
Sensitivity of Retrievals to A Priori Assumptions

Since our retrieved isotopic ratios are somewhat sensitive to the shape of the CH_3CN major isotopologue VMR profile, it is important to investigate the degree to which that profile may depend on any a priori model assumptions. We therefore performed a set of CH_3CN vertical abundance profile retrievals using different a priori profiles, including (1) scaled versions of our default a priori, (2) the CH_3CN profile from M. Dobrijevic & J. Loison (2018), and (3) a gradient profile from A. E. Thelen et al. (2019). As shown in Figure 9, inside the altitudinal region to which our models are sensitive (≈125–500 km), the range where the peak-normalized emission contributions are greater than 1%, we find that the retrieved CH_3CN abundance does not have any significant dependence on the choice of a priori.

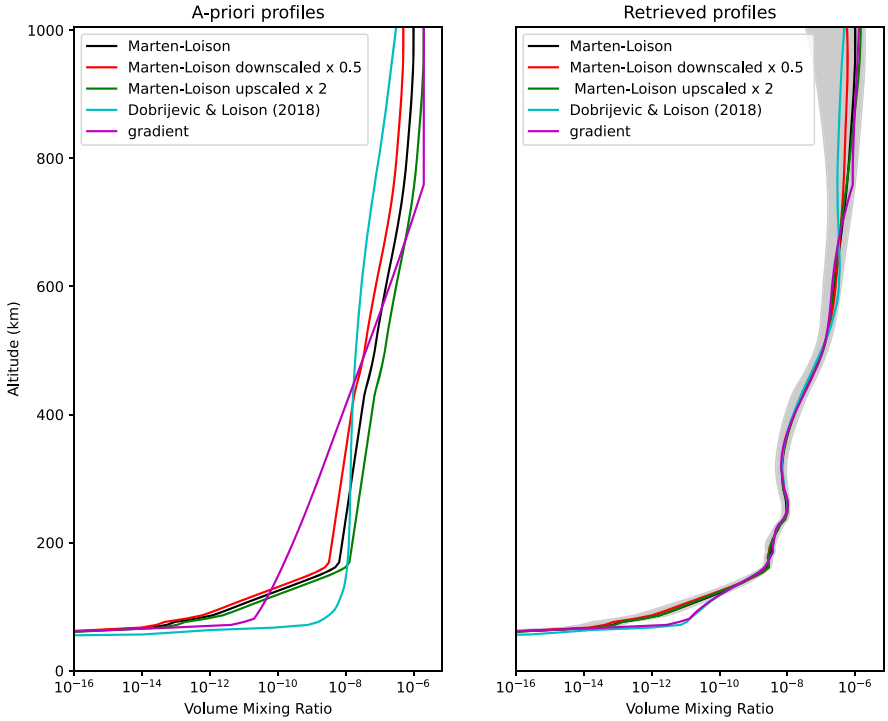

Figure 9. Plot of the a priori (left) and corresponding retrieved profiles (right) to investigate the sensitivity of the retrieved CH_3CN VMR to the shape of the a priori. The retrieved CH_3CN VMR profile (black) is compared against retrievals using scaled versions of our default "Marten–Loison" profile (green and red profiles), the M. Dobrijevic & J. Loison (2018) model profile (cyan), and a log-linear gradient profile (magenta) from A. E. Thelen et al. (2019). The gray shaded region in the right panel is the error on the default CH_3CN retrieved profile.

ORCID iDs

Jonathon Nosowitz https://orcid.org/0009-0004-1366-9472
Martin A. Cordiner https://orcid.org/0000-0001-8233-2436
Conor A. Nixon https://orcid.org/0000-0001-9540-9121
Alexander E. Thelen https://orcid.org/0000-0002-8178-1042
Zbigniew Kisiel https://orcid.org/0000-0002-2570-3154
Nicholas A. Teanby https://orcid.org/0000-0003-3108-5775
Patrick G. J. Irwin https://orcid.org/0000-0002-6772-384X
Steven B. Charnley https://orcid.org/0000-0001-6752-5109
Véronique Vuitton https://orcid.org/0000-0001-7273-1898

References

Altwegg, K., Balsiger, H., Hänni, N., et al. 2020, NatAs, 4, 533
Balucani, N., Skouteris, D., Leonori, F., et al. 2012, JPCA, 116, 10467
Bézard, B., Nixon, C. A., Kleiner, I., & Jennings, D. E. 2007, Icar, 191, 397
Borysow, A., & Frommhold, L. 1986a, ApJ, 303, 495
Borysow, A., & Frommhold, L. 1986b, ApJ, 304, 849
Borysow, A., & Frommhold, L. 1986c, ApJ, 311, 1043
Borysow, A., & Frommhold, L. 1987, ApJ, 318, 940
Borysow, A., & Tang, C. 1993, Icar, 105, 175
Boucher, D., Burie, J., Demaison, J., et al. 1977, JMoSp, 64, 290
Cazzoli, G., & Puzzarini, C. 2006, JMoSp, 240, 153
Choukroun, M., Grasset, O., Tobie, G., & Sotin, C. 2010, Icar, 205, 581
Cordiner, M. A., Garcia-Berrios, E., Cosentino, R. G., et al. 2020, ApJL, 904, L12
Cordiner, M. A., Nixon, C. A., Charnley, S. B., et al. 2018, ApJL, 859, L15
Cordiner, M. A., Palmer, M. Y., Nixon, C. A., et al. 2015, ApJL, 800, L14
Cordiner, M. A., Teanby, N. A., Nixon, C. A., et al. 2019, AJ, 158, 76
Courtin, R., Swinyard, B., Moreno, R., et al. 2011, A&A, 536, L2
Davies, A. G., Sotin, C., Choukroun, M., Matson, D. L., & Johnson, T. V. 2016, Icar, 274, 23
Dobrijevic, M., & Loison, J. 2018, Icar, 307, 371
Dudaryonok, A., Lavrentieva, N., & Buldyreva, J. 2015, Icar, 250, 76
Glein, C. R. 2015, Icar, 250, 570
Gurwell, M. A. 2004, ApJL, 616, L7
Hidayat, T., Marten, A., Bézard, B., et al. 1997, Icar, 126, 170
Hörst, S. M. 2017, JGRE, 122, 432
Hills, R. 2016, Note on Spectral Response V2, NRAO https://safe.nrao.edu/wiki/pub/Main/ALMAWindowFunctions/Note_on_Spectral_Response_V2.pdf
Iino, T., Sagawa, H., & Tsukagoshi, T. 2020, ApJ, 890, 95
Irwin, P., Teanby, N., de Kok, R., et al. 2008, JQSRT, 109, 1136
Jacquinet-Husson, N., Scott, N., Chédin, A., et al. 2005, JQSRT, 95, 429
Jennings, D. E., Nixon, C. A., Jolly, A., et al. 2008, ApJL, 681, L109
Jolly, A., Fayt, A., Benilan, Y., et al. 2010, ApJ, 714, 852
Kossacki, K. J., & Lorenz, R. D. 1996, P&SS, 44, 1029
Kuiper, G. P. 1944, ApJ, 100, 378
Lellouch, E., Gurwell, M. A., Moreno, R., et al. 2019, NatAs, 3, 614
Liang, M.-C., Heays, A. N., Lewis, B. R., Gibson, S. T., & Yung, Y. L. 2007, ApJL, 664, L115
Loison, J., Hébrard, E., Dobrijevic, M., et al. 2015, Icar, 247, 218
MacKenzie, S. M., Birch, S. P. D., Hörst, S., et al. 2021, PSJ, 2, 112
Mandt, K. E., Mousis, O., Lunine, J., & Gautier, D. 2014, ApJL, 788, L24
Mandt, K. E., Waite, J. H., Teolis, B., et al. 2012, ApJ, 749, 160
Marten, A., Hidayat, T., Biraud, Y., & Moreno, R. 2002, Icar, 158, 532
Medvedev, I., Winnewisser, M., De Lucia, F. C., et al. 2004, JMoSp, 228, 314
Molter, E. M., Nixon, C. A., Cordiner, M. A., et al. 2016, AJ, 152, 42
Müller, H. S. P., Drouin, B. J., & Pearson, J. C. 2009, A&A, 506, 1487
Müller, H. S. P., Thorwirth, S., Roth, D. A., & Winnewisser, G. 2001, A&A, 370, L49
Niemann, H. B., Atreya, S. K., Demick, J. E., et al. 2010, JGRE, 115, E12006
Nixon, C., Achterberg, R., Vinatier, S., et al. 2008a, Icar, 195, 778
Nixon, C., Lorenz, R., Achterberg, R., et al. 2018, P&SS, 155, 50
Nixon, C. A. 2024, ESC, 8, 406
Nixon, C. A., Jennings, D. E., Bézard, B., et al. 2008b, ApJL, 681, L101
Nixon, C. A., Temelso, B., Vinatier, S., et al. 2012, ApJ, 749, 159
Nomura, H., Furuya, K., Cordiner, M., et al. 2022, arXiv:2203.10863
Oro, J., Miller, S. L., & Lazcano, A. 1990, AREPS, 18, 317
Palmer, M. Y., Cordiner, M. A., Nixon, C. A., et al. 2017, SciA, 3, e1700022
Rengel, M., Sagawa, H., & Hartogh, P. 2011, New Sub-millimeter Heterodyne Observations of CO and HCN in Titan's Atmosphere with the Apex Swedish Heterodyne Facility Instrument (Singapore: World Scientific), 173
Rengel, M., Sagawa, H., Hartogh, P., et al. 2014, A&A, 561, A4
Rengel, M., Shulyak, D., Hartogh, P., et al. 2022, A&A, 658, A88
Rodgers, C. D. 1976, RvGeo, 14, 609
Serigano, J., Nixon, C. A., Cordiner, M. A., et al. 2016, ApJL, 821, L8
Teanby, N., Irwin, P., Nixon, C., et al. 2013, P&SS, 75, 136
Teanby, N. A., Bézard, B., Vinatier, S., et al. 2017, NatCo, 8, 1586
Teanby, N. A., de Kok, R., Irwin, P. G. J., et al. 2008, JGRE, 113, E12003
Teanby, N. A., Sylvestre, M., Sharkey, J., et al. 2019, GeoRL, 46, 3079
Thelen, A. E., Cordiner, M. A., Nixon, C. A., et al. 2020, ApJL, 903, L22
Thelen, A. E., Nixon, C., Chanover, N., et al. 2019, Icar, 319, 417
Thelen, A. E., Nixon, C. A., Cordiner, M. A., et al. 2024, PSJ, 5, 125
Tobie, G., Lunine, J. I., & Sotin, C. 2006, Natur, 440, 61
Vinatier, S., Bézard, B., & Nixon, C. A. 2007, Icar, 191, 712
Vuitton, V., Yelle, R., Klippenstein, S., Hörst, S., & Lavvas, P. 2019, Icar, 324, 120
Willacy, K., Allen, M., & Yung, Y. 2016, ApJ, 829, 79
Wilson, E. H., & Atreya, S. K. 2004, JGRE, 109, E06002